

“Forbidden” phonon: dynamical signature of bond symmetry breaking in the iron chalcogenides

David M. Fobes,^{1,*} Igor A. Zaliznyak,^{1,†} John M. Tranquada,¹ Zhijun Xu,¹ Genda Gu,¹ Xu-Gang He,¹ Wei Ku,¹ Yang Zhao,^{2,3} Masaaki Matsuda,⁴ V. Ovidiu Garlea,⁴ and Barry Winn⁴

¹*CMPMSD, Brookhaven National Laboratory, Upton, NY 11973 USA*

²*NIST Center for Neutron Research, National Institute of Standards and Technology, Gaithersburg, Maryland 20899, USA*

³*DMSE, University of Maryland, College Park, MD 20742 USA*

⁴*QCMD, Oak Ridge National Laboratory, Oak Ridge, TN 37831 USA*

(Dated: May 11, 2016)

Investigation of the inelastic neutron scattering spectra in $\text{Fe}_{1+y}\text{Te}_{1-x}\text{Se}_x$ near a signature wave vector $\mathbf{Q} = (1, 0, 0)$ for the bond-order wave (BOW) formation of parent compound Fe_{1+y}Te [1] reveals an acoustic-phonon-like dispersion present in all structural phases. While a structural Bragg peak accompanies the mode in the low-temperature phase of Fe_{1+y}Te , it is absent in the high-temperature tetragonal phase, where Bragg scattering at this \mathbf{Q} is forbidden by symmetry. Notably, this mode is also observed in superconducting $\text{FeTe}_{0.55}\text{Se}_{0.45}$, where structural and magnetic transitions are suppressed, and no BOW has been observed. The presence of this “forbidden” phonon indicates that the lattice symmetry is dynamically or locally broken by magneto-orbital BOW fluctuations, which are strongly coupled to lattice in these materials.

PACS numbers: 71.27.+a 74.70.Xa 75.40.Gb

Since the discovery of high-temperature superconductivity (HTSC) in cuprates, elucidation of the connection between the electronic and lattice degrees of freedom has been of considerable interest in regard to the driving mechanisms behind HTSC. The iron-based superconductors (FeSCs) share many similarities with the cuprates; both have parent phases featuring antiferromagnetic (AFM) ordering, structural distortions, strong magnetic fluctuations and broken electronic symmetry [1–5]. Understanding the complex lattice dynamics in FeSCs is of critical importance for understanding the connection between these different orders, their relation to the superconductivity, and the connection between the two types of HTSCs. The compounds in the iron-chalcogenide series, featuring the simplest structure and the strongest electronic correlation among the Fe-HTSC, provide a good opportunity to study these dynamics.

The iron-chalcogenides $\text{Fe}_{1+y}\text{Te}_{1-x}\text{Se}_x$, with a maximum T_c of ~ 14.5 K at optimal doping, consist of a continuous stacking of Fe square-lattice layers, separated by two half-filled chalcogen (Te,Se) layers [6–8]. Initially predicted by band structure calculations to be a metal [9], the non-superconducting parent material Fe_{1+y}Te instead exhibits non-metallic character in resistivity, indicative of charge carrier incoherence near the Fermi level at high temperatures [10–12]. Large local magnetic moments of about $4 \mu_B$, which indicate full involvement of three electronic bands, are revealed by Curie-Weiss behavior in magnetic susceptibility [11–13]; nevertheless, angle-resolved photoemission (ARPES) studies show significant spectral weight near the Fermi energy [14–16].

These electronic and magnetic properties of $\text{Fe}(\text{Te},\text{Se})$ are very sensitive to non-stoichiometric Fe at interstitial sites, particularly evident in the parent compound [17–

24]; at low concentrations, a first-order magnetostructural transition is observed from paramagnetic tetragonal ($P4/nmm$) to monoclinic ($P2_1/m$) with bicollinear AFM order (propagation vector $\mathbf{q} = (0.5, 0, 0.5)$) and metallic resistivity [18–21]. For intermediate $0.06 \lesssim y \lesssim 0.12$ the magneto-structural transition splits into a sequence of transitions. Our recent neutron studies of Fe_{1+y}Te in the intermediate range uncovered evidence that the lowest-temperature transition coincides with the formation of a bond-order wave (BOW), indicative of ferro-orbital order in the ground state [1], which stabilizes the bicollinear AFM order in the low- T phase, common to $y \lesssim 0.12$.

In this letter, we report inelastic neutron scattering measurements on $\text{Fe}_{1+y}\text{Te}_{1-x}\text{Se}_x$ samples, aimed at elucidating the dynamics associated with the newly discovered BOW state. We have studied two compositions of the Fe_{1+y}Te parent compound, as well as the optimally-doped superconductor $\text{FeTe}_{1-x}\text{Se}_x$ ($x = 0.45$). In all three samples, we observe an acoustic-phonon-like mode that appears to disperse out of the $\mathbf{Q} = (1, 0, 0)$ reciprocal lattice point, even in the tetragonal structure where such a Bragg peak is forbidden by crystal symmetry; only a weak reflection, manifest of the BOW state, develops at this wave vector in the parent compounds at low T . At all temperatures, the mode appears to be ungapped and sharp within instrumental resolution, demonstrating it is not a conventional soft mode; furthermore, we have confirmed that it is not a result of magnetic spin-flip scattering. The presence of this phonon suggests a dynamical breaking of crystal symmetry, potentially related to the magneto-orbital BOW fluctuations in these materials.

Neutron scattering measurements were carried out using the Hybrid Spectrometer (HYSPEC) [25, 26] at the Spallation Neutron Source, Oak Ridge National Labo-

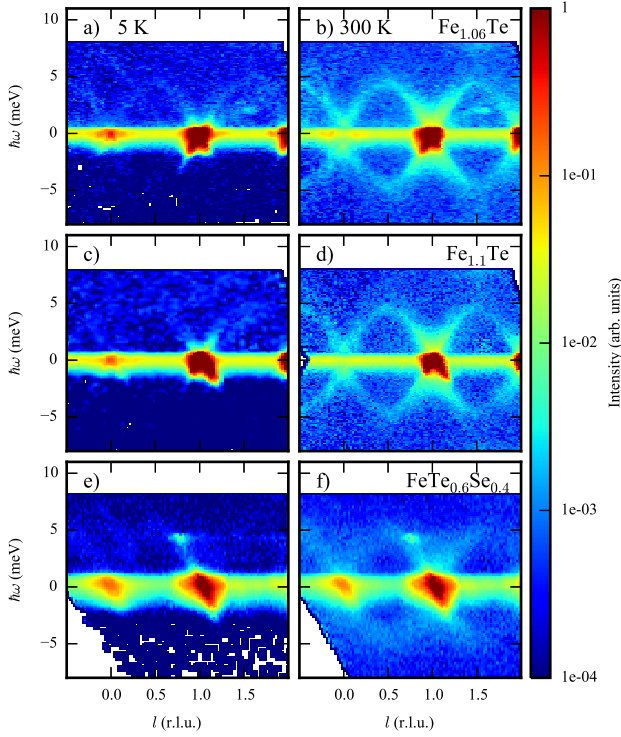


FIG. 1. (Color Online) Neutron scattering intensity along $(1,0,l)$ as a function of energy transfer $\hbar\omega$, showing the phonon dispersions from (100) , (101) and (102) at 5 K (left column) and 300 K (right column) for (a–b) $\text{Fe}_{1.06}\text{Te}$, (c–d) $\text{Fe}_{1.1}\text{Te}$, and (e–f) $\text{FeTe}_{0.55}\text{Se}_{0.45}$.

ratory, and polarized neutron measurements were performed on the Double Focusing Triple-Axis Spectrometer (BT-7) [27] at the NIST Center for Neutron Research and the Polarized Triple-Axis Spectrometer (HB-1) at the High-Flux Isotope Reactor (HFIR) at Oak Ridge National Laboratory ($E_f = 14.7$ meV). The three following samples were investigated: $\text{Fe}_{1.06}\text{Te}$, $\text{Fe}_{1.1}\text{Te}$, and $\text{FeTe}_{0.55}\text{Se}_{0.45}$. $\text{Fe}_{1.06}\text{Te}$ consists of two co-aligned single crystals ($m_{\text{total}} \approx 24$ g) with a mosaic of 2.7° full width at half maximum (FWHM). $\text{Fe}_{1.1}\text{Te}$ is a single crystal ($m = 18.45$ g) with a mosaic of 2.2° FWHM. $\text{FeTe}_{0.55}\text{Se}_{0.45}$ is a single crystal ($m = 23.4$ g) with a mosaic of 2.2° FWHM. All samples were grown by the horizontal Bridgman method [8], and mounted on an aluminum holder. Measurements of scattering in the $(h,k,0)$ and the $(h,0,l)$ plane were obtained by aligning crystals with c -axis, or b -axis vertical, respectively.

In Fig. 1, we present inelastic neutron scattering intensity, which reveals acoustic-phonon-like dispersions along $(1,0,l)$, as a function of energy transfer $\hbar\omega$, for all three samples. At 5 K the structure in the Fe_{1+y}Te samples is monoclinic ($P2_1/m$) [1], and acoustic phonons dispersing out of the (100) and (101) Bragg peaks present at these positions would not be unexpected (Fig. 1a, 1c). However, at 300 K the structure is tetragonal ($P4/nmm$) [18] and the (100) Bragg reflection is symmetry-forbidden; nevertheless, a gapless, acoustic-phonon-like mode is still

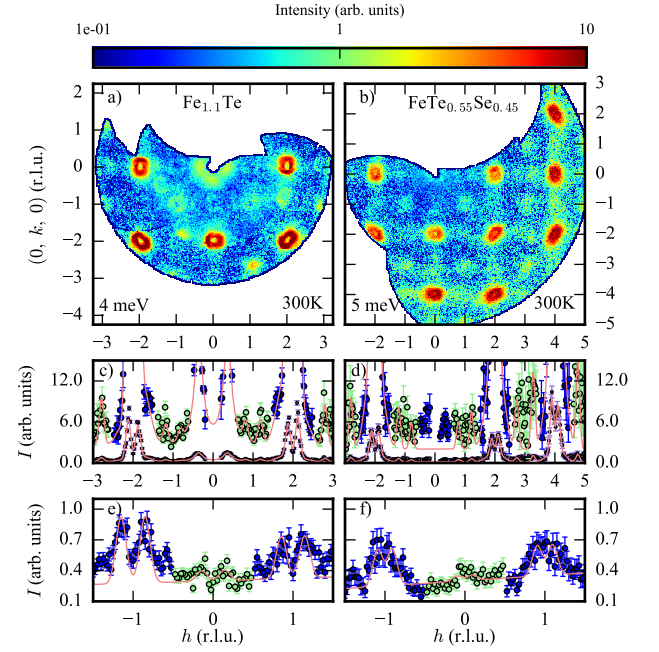


FIG. 2. (Color Online) The inelastic neutron scattering intensity maps at $\hbar\omega = 4.0(5)$ meV in $\text{Fe}_{1.1}\text{Te}$ (a) and $\hbar\omega = 5(1)$ meV in $\text{FeTe}_{0.55}\text{Se}_{0.45}$ (b) in the $(h,k,0)$ zone, measured on HYSPEC using $E_i = 24$ meV and $E_i = 50$ meV, respectively. Panels (c) and (d) show the longitudinal and (e) and (f) the transverse line cuts of the data in (a) and (b), respectively, across the symmetry equivalent forbidden Bragg positions. The lines are Gaussian fits, revealing the longitudinal phonon velocities near $(2,0,0)$, $v_L = 36(2)$ meV/r.l.u. in $\text{Fe}_{1.1}\text{Te}$ and $v_L = 44(8)$ meV/r.l.u. in $\text{FeTe}_{0.55}\text{Se}_{0.45}$, compared to $v = 21(1)$ meV/r.l.u. and $v = 22(2)$ meV/r.l.u., respectively, for the forbidden mode [r.l.u. is in units of $a^* = 1.645(5)\text{\AA}^{-1}$].

observed dispersing out of the forbidden Bragg position (Fig. 1b, 1d). A similar mode is also observed in superconducting $\text{FeTe}_{0.55}\text{Se}_{0.45}$ throughout the whole temperature range (Figs. 1e–1f). In $\text{FeTe}_{0.55}\text{Se}_{0.45}$ the structural and magnetic transitions observed in the parent compound are suppressed, and it is therefore tetragonal at all temperatures, so that Bragg scattering at (100) is never allowed. In Figs. 1e–1f, residual elastic scattering appears to be present at (100) , but elastic slices (data not shown) reveal an unusual structure to the (100) peak, which changes depending on the incident energy, suggesting that these elastic features are a result of multiple scattering, not uncommon in samples of this size. The observed forbidden mode appears to be ungapped within the experimental limit, $\lesssim 1$ meV, mainly imposed by the presence of this spurious double scattering.

In Fig. 2 we show constant-energy inelastic data covering a large region of the $(h,k,0)$ plane for the $\text{Fe}_{1.1}\text{Te}$ and $\text{FeTe}_{0.55}\text{Se}_{0.45}$ samples. The data reveal the presence of ring-like contours of inelastic scattering intensity consistent with the dispersion of excitations around the forbidden Bragg peaks at the symmetry equivalent positions in different Brillouin zones, $(\pm 2n \pm 1, 0, 0)$, $(0, -2n - 1, 0)$,

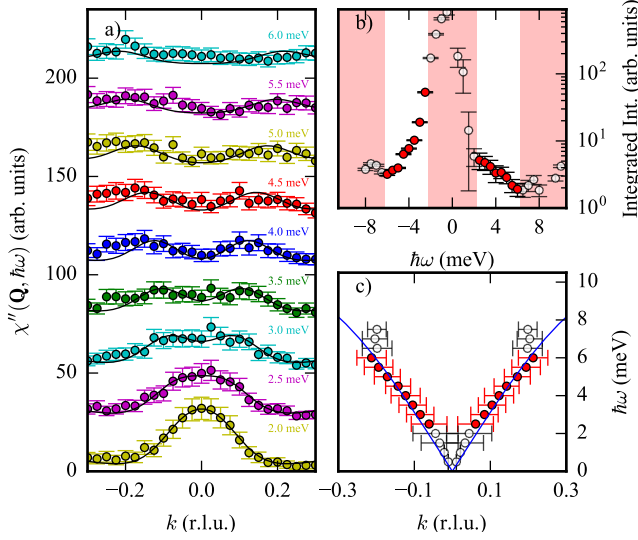


FIG. 3. (Color Online) (a) $\chi''(\mathbf{Q}, \hbar\omega)$ line scans along $(1, k, 0)$ at energy transfers between 2 meV and 6 meV at 300 K of the $\text{FeTe}_{0.55}\text{Se}_{0.45}$ sample, fitted with two Gaussians symmetric around $k = 0$. Data are shifted for clarity. (b) Integrated peak intensity as a function of energy, obtained from fitting. (c) Phonon dispersion in energy fitted to $\hbar\omega = v|\sin(\pi k/2)|$ (solid line). Shaded regions in (b) and open symbols in (b) and (c) indicate regions where fitting is least reliable.

$n = 0, 1, 2$. The line cuts presented in Fig. 2c, 2d, reveal both the longitudinal acoustic phonon branch near $(\pm 2n, 0, 0)$ and the small “forbidden mode” peaks near $(\pm 2n + 1, 0, 0)$, whose intensity distribution with respect to the wave vector direction is consistent with that of a longitudinal acoustic phonon, as discussed in more detail below. However, the forbidden peak position reveals a dispersion with velocity, $v = 21(1)$ meV/r.l.u. in $\text{Fe}_{1.1}\text{Te}$ and $v = 22(2)$ meV/r.l.u. in $\text{FeTe}_{0.55}\text{Se}_{0.45}$, which is markedly (nearly twice) slower than the respective longitudinal phonon velocities, $v_L \approx 36(2)$ meV/r.l.u. and $v_L = 44(8)$ meV/r.l.u., and is close to that of the transverse acoustic modes. Hence, the combination of polarization and dispersion of the forbidden mode is inconsistent with that expected for a phonon in an ideal lattice. In addition, the forbidden phonon intensities at symmetry equivalent positions do not display the expected scaling with wave vector, $\sim Q^2$; one should expect that the position-normalized phonon intensity at symmetry-equivalent positions, I/Q^2 , should be constant as a function of Q , whereas we observe a significant decrease [28].

In Fig. 3, we present a set of line-cuts along $(1, k, 0)$ of $\chi''(\mathbf{Q}, \hbar\omega)$ in $\text{FeTe}_{0.55}\text{Se}_{0.45}$ at multiple energy transfers, $2 \text{ meV} \leq \hbar\omega \leq 6 \text{ meV}$ (Fig. 3a), which we use for an analysis of the transverse acoustic-phonon-like dispersion near (100) (Fig. 1f). Line cuts were fit to a two-Gaussian function, where the Gaussians were constrained to be symmetric around $k = 0$. Figures 3b–3c show the results of fitting, the total integrated intensity and dispersion, respectively. The dispersion is fit to $\hbar\omega = v|\sin(\pi k)|$,

yielding the acoustic velocity $\pi v = 32(2)$ meV/r.l.u.

The neutron scattering cross-section of a phonon mode with index ν and wave vector \mathbf{q} measured at a wave vector $\mathbf{Q} = \mathbf{q} + \boldsymbol{\tau}$ near the reciprocal lattice vector $\boldsymbol{\tau}$ and at a temperature T ,

$$\frac{d^2\sigma}{dE d\Omega} = N \frac{k_f}{k_i} |\mathbf{Q} \cdot \mathbf{g}_{\mathbf{Q}}^\nu|^2 \frac{\hbar}{2\omega_\nu(\mathbf{q})} \frac{\delta(\hbar\omega - \hbar\omega_\nu(\mathbf{q}))}{1 - e^{-\hbar\omega/T}}, \quad (1)$$

is proportional to the square of the structure factor,

$$\mathbf{g}_{\mathbf{Q}}^\nu = \sum_j \frac{b_j}{\sqrt{M_j}} e^{-W_j(\mathbf{Q})} e^{i\mathbf{Q} \cdot \mathbf{r}_j} \boldsymbol{\xi}_j^\nu(\mathbf{q}), \quad (2)$$

where $e^{-2W_j(\mathbf{Q})}$ and b_j are the Debye-Waller factor and the scattering length of an atom of mass M_j at a position \mathbf{r}_j in the unit cell (N is the number of unit cells); $\omega_\nu(\mathbf{q}) = \omega_\nu(\mathbf{q} + \boldsymbol{\tau})$ and $\boldsymbol{\xi}_j^\nu(\mathbf{q}) = \boldsymbol{\xi}_j^\nu(\mathbf{q} + \boldsymbol{\tau})$ are the mode frequency and polarization vectors, which are given by the eigenvalues and the eigenvectors of the dynamical matrix [29, 30]. Due to lattice periodicity, \mathbf{q} can be constrained to the first Brillouin zone.

In the long-wavelength limit of acoustic phonons, all atoms in the unit cell move uniformly together, and the magnitude of the phonon structure factor approaches that of the static structure factor at the Bragg position, $\boldsymbol{\tau}$, from which the dispersion originates, $|\mathbf{g}_{\mathbf{Q}}^\nu \cdot \mathbf{Q}|^2 \xrightarrow{\mathbf{Q} \rightarrow \boldsymbol{\tau}} (\tau^2/M) |F(\boldsymbol{\tau})|^2 \cos^2 \beta$, where M is the sum of the atomic masses and β is the angle that the phonon polarization makes with $\boldsymbol{\tau}$. Therefore, in the situation where $\boldsymbol{\tau}$ is a forbidden Bragg reflection, $|F(\boldsymbol{\tau})| = 0$ and acoustic phonon scattering is forbidden in this approximation. Using a Taylor expansion about $\mathbf{Q} = \boldsymbol{\tau} + \mathbf{q}$ near $\boldsymbol{\tau}$, we obtain, $|\mathbf{g}_{\mathbf{Q}}^\nu|^2 \lesssim \alpha q^2$. Thus, taking account of the linear dispersion of an acoustic mode at small q , the one-phonon scattering intensity converted to $\chi''(\mathbf{Q}, \omega)$ by adjusting for the thermal balance factor in Eq. (1), which is proportional to $|\mathbf{g}_{\mathbf{Q}}^\nu|^2 / \omega_\nu(q) \lesssim \alpha q / v$, should be decreasing to zero, at most linearly in q , as $q \rightarrow 0$ and $\hbar\omega \rightarrow 0$. This is in contradiction to what is seen in Fig. 3b, where the integrated intensity of $\chi''(\mathbf{Q}, \omega)$, increases as $\hbar\omega$ decreases. Analysis of $\text{Fe}_{1.1}\text{Te}$ and $\text{Fe}_{1.06}\text{Te}$ data (Figs. 1a–1d) leads to similar conclusions [28].

In order to understand the possible origin of the observed “forbidden phonon” mode, we performed LDA frozen phonon calculations, which reveal a coupling between atomic displacements and a spin imbalance of neighboring Fe atoms, suggesting the possibility that a forbidden phonon mode could result from magnetic scattering induced by thermal atomic vibrations [28]. To test this, polarized neutron measurements were performed on the $\text{Fe}_{1.06}\text{Te}$ sample, as shown in Fig. 4, where spin-flip (SF) and non-spin flip (NSF) scattering was measured at 300 K and 2.5 K using ^3He polarizers and $\mathbf{Q} \parallel \mathbf{B}$ (guide field). With a median flipping ratio of ~ 30 during these experiments, our results indicate a lack of SF magnetic scattering from either the expected (200) phonon or the

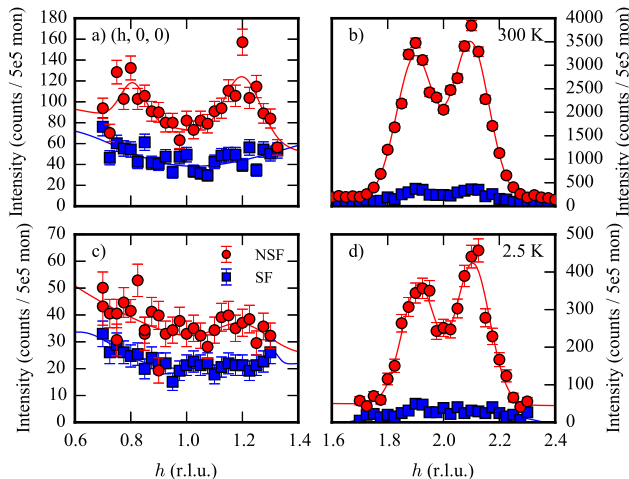


FIG. 4. (Color Online) Polarized inelastic neutron scattering line scans along $(h, 0, 0)$ around $(1, 0, 0)$ (left column) and $(2, 0, 0)$ (right column) at 300 K (top row) and 2.5 K (bottom row) in the non-spin-flip (circle) and spin-flip (square) channels of the $\text{Fe}_{1.06}\text{Te}$ sample, measured at BT-7.

“forbidden” (100) mode. A similar polarized neutron experiment was performed on the $\text{FeTe}_{0.55}\text{Se}_{0.45}$ sample [28] at HB-1, yielding consistent results. While the absence of spin-flip scattering indicates the mode primarily originates from atomic displacements, this does not exclude a scenario in which the atomic displacements originate from magnetic/orbital fluctuations, as we discuss below.

A previous example of a “forbidden” phonon was found in $\text{Fe}_{65}\text{Ni}_{35}$ invar, in which a transverse acoustic (TA) mode is observed in a position where it is forbidden by the scattering geometry, *i.e.* $\mathbf{Q} \cdot \boldsymbol{\xi}(\mathbf{q}) = 0$, cf. Eqs. (1–2) [31]. An early explanation suggested this mode could result from the breaking of the cubic crystal symmetry of the dynamical matrix by slow local orthorhombic distortions [32]. However, this mode has several properties divergent from those expected for a conventional phonon. The mode does not exhibit the expected Q^2 -dependence, but instead shows a decrease in intensity at higher Q . The mode also shows a significant *decrease* in intensity at temperatures well above the magnetic ordering temperature ($T_c \approx 550$ K). Finally, there is a polarization ratio associated with this mode, where some contribution to the mode is structural and some is magnetic [33]. These results suggested that the scattering intensity is in part a result of magnetic scattering, but the strong coupling of the magnetic and lattice degrees of freedom also results in magnetically-driven structural phonon scattering.

The magnetic fluctuations in the iron chalcogenides are well known to be strong, even in the absence of long-range magnetic order in these materials [34, 35], and previous studies have emphasized the strong coupling between the electronic spin, orbital, and lattice degrees of freedom [1]. The location of the “forbidden” phonon, which we observe near the wave vector of ferro-orbital ordering in

the parent FeTe material [1] clearly suggests involvement of the orbital degrees of freedom. This is consistent with the magneto-vibrational scenario set forth by our LDA frozen phonon calculation, similar to the scenario offered to explain the “forbidden” phonon in Fe-Ni invar, but with an additional factor of the orbital hybridization, a crucial ingredient. Specifically, fluctuations of the orbital/magnetic nature associated with the spin imbalance between neighboring Fe atoms might lead to vibrations of forbidden character [28].

Recently, another example of a “forbidden” phonon has been observed in $\text{La}_{2-x}\text{Ba}_x\text{CuO}_4$ ($x = 0.125$), where the mode has been attributed to CuO_6 octahedral tilt fluctuations [36]. A possible electronic coupling for the observed mode is not ruled out. It could be that an acoustic phonon-like mode near a structurally forbidden Bragg reflection is a universal feature indicative of coupling between electronic and lattice degrees of freedom in both cuprates and iron chalcogenides.

In summary, we have observed an acoustic phonon-like mode dispersing from a position where Bragg scattering is forbidden by crystal symmetry in both the non-superconducting end-member and optimally-doped superconducting member of the iron-chalcogenide family. The mode intensity does not follow the expected behavior for phonon scattering near a forbidden Bragg reflection. Frozen phonon LDA calculations suggest that this mode might originate from slow electronic magnetic/orbital fluctuations associated with Fe spin moments leading to a dynamical breaking of the crystal unit cell symmetry.

Work at BNL was supported by Office of Basic Energy Sciences (BES), Division of Materials Sciences and Engineering, U.S. Department of Energy (DOE), under Contract No. DE-SC00112704. Research conducted at ORNL’s Spallation Neutron Source and High Flux Isotope Reactor was sponsored by the Scientific User Facilities Division, Office of Basic Energy Sciences, US Department of Energy. We acknowledge the support of NIST, US Department of Commerce, in providing the neutron research facilities used in this work.

* dfobes@bnl.gov

† zaliznyak@bnl.gov

- [1] D. Fobes, I. A. Zaliznyak, Z. Xu, R. Zhong, G. Gu, J. M. Tranquada, L. Harriger, D. Singh, V. O. Garlea, M. Lumsden, and B. Winn, *Phys. Rev. Lett.* **112**, 187202 (2014).
- [2] D. J. Scalapino, *Rev. Mod. Phys.* **84**, 1383 (2012).
- [3] P. Dai, J. Hu, and E. Dagotto, *Nature Physics* **8**, 709 (2012).
- [4] M. D. Lumsden and A. D. Christianson, *J. Phys. Condens. Matter* **22**, 203203 (2010).
- [5] I. R. Fisher, L. Degiorgi, and Z. X. Shen, *Rep. Prog. Phys.* **74**, 124506 (2011).
- [6] K.-W. Yeh, T.-W. Huang, Y. I. Huang, T.-K. Chen, F.-

- C. Hsu, P. M. Wu, Y.-C. Lee, Y.-Y. Chu, C.-L. Chen, J.-Y. Luo, D.-C. Yan, and M.-K. Wu, *Europhys. Lett.* **84**, 37002 (2008).
- [7] F.-C. Hsu, J.-Y. Luo, K.-W. Yeh, T.-K. Chen, T.-W. Huang, P.-M. Wu, Y.-C. Lee, Y.-L. Huang, Y.-Y. Chu, D.-C. Yan, and M.-K. Wu, *Proc. Natl. Acad. Sci. U.S.A.* **105**, 14262 (2008).
- [8] J. Wen, G. Xu, G. Gu, J. M. Tranquada, and R. J. Birgeneau, *Rep. Prog. Phys.* **74**, 124503 (2011).
- [9] D. J. Singh, *Sci. Technol. Adv. Mater.* **13**, 054304 (2012).
- [10] T. J. Liu, X. Ke, B. Qian, J. Hu, D. Fobes, E. K. Vehstedt, H. Pham, J. H. Yang, M. H. Fang, L. Spinu, P. Schiffer, Y. Liu, and Z. Q. Mao, *Phys. Rev. B* **80**, 174509 (2009).
- [11] G. F. Chen, Z. G. Chen, J. Dong, W. Z. Hu, G. Li, X. D. Zhang, P. Zheng, J. L. Luo, and N. L. Wang, *Phys. Rev. B* **79**, 140509(R) (2009).
- [12] R. Hu, E. S. Bozin, J. B. Warren, and C. Petrovic, *Phys. Rev. B* **80**, 214514 (2009).
- [13] I. A. Zaliznyak, Z. J. Xu, J. S. Wen, J. M. Tranquada, G. D. Gu, V. Solovyov, V. N. Glazkov, A. I. Zheludev, V. O. Garlea, and M. B. Stone, *Phys. Rev. B* **85**, 085105 (2012).
- [14] Y. Xia, D. Qian, L. Wray, D. Hsieh, G. F. Chen, J. L. Luo, N. L. Wang, and M. Z. Hasan, *Phys. Rev. Lett.* **103**, 037002 (2009).
- [15] Y. Zhang, F. Chen, C. He, L. X. Yang, B. P. Xie, Y. L. Xie, X. H. Chen, M. Fang, M. Arita, K. Shimada, H. Namatame, M. Taniguchi, J. P. Hu, and D. L. Feng, *Phys. Rev. B* **82**, 165113 (2010).
- [16] Z. K. Liu, R.-H. He, D. H. Lu, M. Yi, Y. L. Chen, M. Hashimoto, R. G. Moore, S.-K. Mo, E. A. Nowadnick, J. Hu, T. J. Liu, Z. Q. Mao, T. P. Devereaux, Z. Hussain, and Z.-X. Shen, *Phys. Rev. Lett.* **110**, 037003 (2013).
- [17] T. M. McQueen, Q. Huang, V. Ksenofontov, C. Felser, Q. Xu, H. Zandbergen, Y. S. Hor, J. Allred, A. J. Williams, D. Qu, J. Checkelsky, N. P. Ong, and R. J. Cava, *Phys. Rev. B* **79**, 014522 (2009).
- [18] W. Bao, Y. Qiu, Q. Huang, M. A. Green, P. Zajdel, M. R. Fitzsimmons, M. Zhernenkov, S. Chang, M. Fang, B. Qian, E. K. Vehstedt, J. Yang, H. M. Pham, L. Spinu, and Z. Q. Mao, *Phys. Rev. Lett.* **102**, 247001 (2009).
- [19] E. E. Rodriguez, C. Stock, P. Zajdel, K. L. Krycka, C. F. Majkrzak, P. Zavalij, and M. A. Green, *Phys. Rev. B* **84**, 064403 (2011).
- [20] S. Li, C. de la Cruz, Q. Huang, Y. Chen, J. W. Lynn, J. Hu, Y.-L. Huang, F.-C. Hsu, K.-W. Yeh, M.-K. Wu, and P. Dai, *Phys. Rev. B* **79**, 054503 (2009).
- [21] A. Martinelli, A. Palenzona, M. Tropeano, C. Ferdeghini, M. Putti, M. R. Cimberle, T. D. Nguyen, M. Affronte, and C. Ritter, *Phys. Rev. B* **81**, 094115 (2010).
- [22] C. Stock, E. E. Rodriguez, M. A. Green, P. Zavalij, and J. A. Rodriguez-Rivera, *Phys. Rev. B* **84**, 045124 (2011).
- [23] S. Rössler, D. Cherian, W. Lorenz, M. Doerr, C. Koz, C. Curfs, Y. Prots, U. K. Rössler, U. Schwarz, S. Elizabeth, and S. Wirth, *Phys. Rev. B* **84**, 174506 (2011).
- [24] X. Liu, C.-C. Lee, Z. J. Xu, J. S. Wen, G. Gu, W. Ku, J. M. Tranquada, and J. P. Hill, *Phys. Rev. B* **83**, 184523 (2011).
- [25] I. Zaliznyak, V. Ghosh, S. Shapiro, and L. Passell, *Physica B: Condensed Matter* **356**, 150 (2005).
- [26] B. Winn, U. Filges, V. O. Garlea, M. Graves-Brook, M. Hagen, C. Jiang, M. Kenzelmann, L. Passell, S. M. Shapiro, X. Tong, and I. Zaliznyak, *EPJ Web of Conferences* **83**, 03017 (2015).
- [27] J. Lynn, Y. Chen, S. Chang, Y. Zhao, S. Chi, I. Ratcliff, W., B. Ueland, and R. Erwin, *J. Res. Natl. Inst. Stand. Technol.* **117**, 61 (2012).
- [28] See Supplemental Material for additional details of structural model, fitting, and determination of double scattering.
- [29] B. N. Brockhouse and P. K. Iyengar, *Phys. Rev.* **111**, 747 (1958).
- [30] R. J. Elliott and M. F. Thorpe, *Proc. Phys. Soc.* **91**, 903 (1967).
- [31] P. J. Brown, I. K. Jassim, K.-U. Neumann, and K. R. A. Ziebeck, *Physica B* **161**, 9 (1989).
- [32] S. Lipiński, K.-U. Neumann, and K. R. A. Ziebeck, *J. Phys.: Condens. Matter* **6**, 9773 (1994).
- [33] P. J. Brown, R. Roessli, J. G. Smith, K.-U. Neumann, and K. R. A. Ziebeck, *J. Phys.: Condens. Matter* **8**, 1527 (1996).
- [34] I. A. Zaliznyak, Z. Xu, J. M. Tranquada, G. Gu, A. M. Tsvetlik, and M. B. Stone, *Phys. Rev. Lett.* **107**, 216403 (2011).
- [35] I. Zaliznyak, A. T. Savici, M. Lumsden, A. Tsvetlik, R. Hu, and C. Petrovic, *Proc. Natl. Acad. Sci. USA.* **112**, 10316 (2015).
- [36] E. S. Bozin, R. Zhong, K. R. Knox, G. Gu, J. P. Hill, J. M. Tranquada, and S. J. L. Billinge, *Phys. Rev. B* **91**, 054521 (2015).

Supplementary Material

“Forbidden” phonon: dynamical signature of bond symmetry breaking in the iron-chalcogenides

David M. Fobes,^{1,*} Igor A. Zaliznyak,^{1,†} Zhijun Xu,¹ Genda Gu,¹ Xu-Gang He,¹ Wei Ku,¹ John M. Tranquada,¹ Yang Zhao,^{2,3} Masaaki Matsuda,⁴ V. Ovidiu Garlea,⁴ and Barry Winn⁴

¹*CMPMSD, Brookhaven National Laboratory, Upton, NY 11973 USA*

²*NIST Center for Neutron Research, National Institute of Standards and Technology, Gaithersburg, Maryland 20899, USA*

³*DMSE, University of Maryland, College Park, MD 20742 USA*

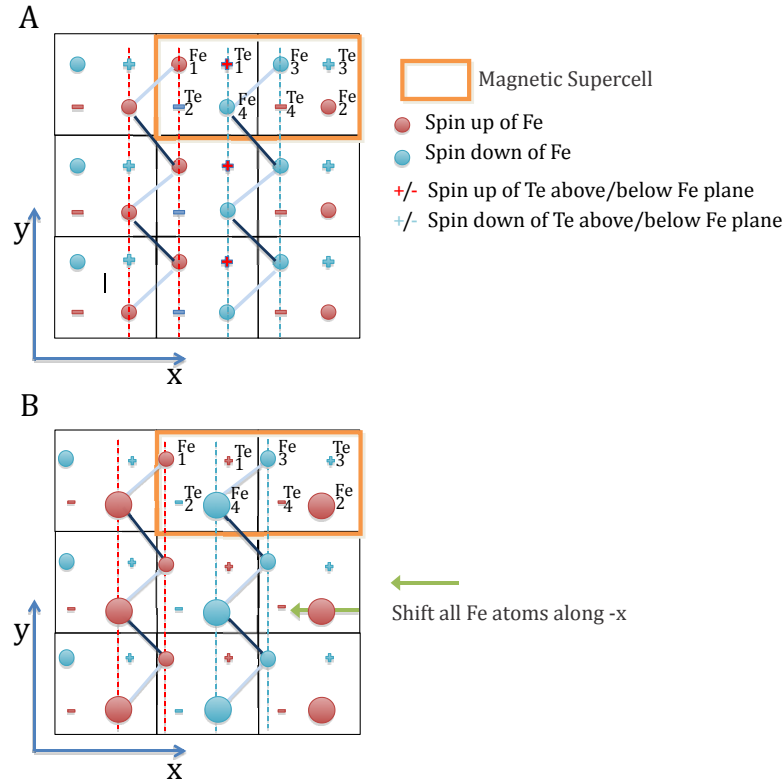
⁴*QCMD, Oak Ridge National Laboratory, Oak Ridge, TN 37831 USA*

1. Frozen phonon calculation for FeTe

Here we present the results of the frozen phonon calculations, which demonstrate strong coupling between fluctuations of the total magnetic moment localized on Fe atoms and their atomic displacements. LDA+U calculations were performed based on the magnetic super-cell, which includes 4 Fe and 4 Te atoms, corresponding to the bicollinear antiferromagnetic structure of parent compound FeTe (Fig. S1A). An effective on-site Coulomb interaction of $U=2$ eV and effective on-site exchange interaction of $J=0.8$ eV were used. In order to elucidate the relationship between iron local-spin moments and acoustic phonons, we shift Fe atoms along the $-x$ direction, as illustrated in Fig. S1B and S3a, and compute the resulting magnetic moments on Fe and Te atoms. The results are listed in Table 1 and summarized in Fig. S2. We observe that the local magnetic moments on the Fe atoms change nearly linearly with the shift in their atomic positions. We see that a significant, up to 8% (in units of lattice spacing) shift of Fe atomic positions is associated with only a small, $\sim \pm 0.06 \mu_B$ imbalance in the magnetic moments. From the calculations, it also appears that small anisotropic effects exist due to the out-of-plane Te atoms, and they also bear small, position-dependent magnetic moments. From here we conclude that small fluctuations of magnetic moments can result in significant nuclear displacements detectable by neutron scattering.

Table 1. Summary of the results of the frozen phonon calculations in FeTe.

Atoms in SC	M (0% Shift)	M (-x) (1% Shift)	M (-x) (2% Shift)	M (-x) (4% Shift)	M (-x) (8% Shift)
Fe1	2.62025	2.61165	2.60654	2.59396	2.56181
Fe2	2.62026	2.61205	2.60723	2.59537	2.55145
Fe3	-2.62025	-2.61165	-2.60654	-2.59396	-2.56181
Fe4	-2.62026	-2.61205	-2.60723	-2.59537	-2.55145
Te1	0.00161	0.00221	0.00281	0.00408	0.00626
Te2	-0.00161	-0.00153	-0.00135	-0.00119	-0.00038
Te3	-0.00161	-0.00221	-0.00281	-0.00408	-0.00626
Te4	0.00161	0.00153	0.00135	0.00119	0.00038

**Figure S1.** Schematics of the crystal structure of FeTe. The rectangular supercell corresponding to the bicollinear magnetic structure contains four different Fe and Te sites. Zig-zag lines connect the equivalent Fe sites in the static low-temperature structure.

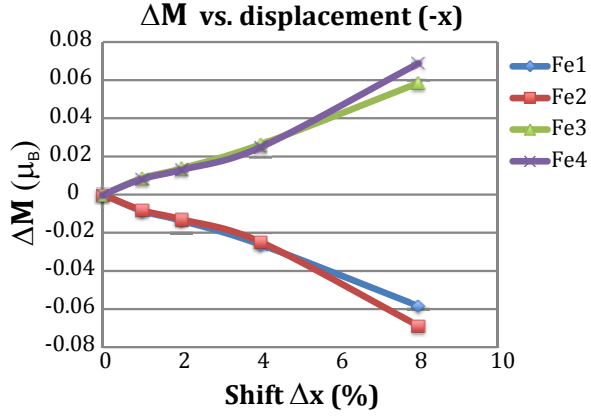


Figure S2. Change in the spin magnetic moment of Fe atoms as a function of displacement from the equilibrium shown in Fig. S1B.

2. Characterization of magnetic scattering in $\text{Fe}_{1.06}\text{Te}$, $\text{Fe}_{1.1}\text{Te}$ and $\text{FeTe}_{0.55}\text{Se}_{0.55}$ samples

Here we present inelastic data that provide characterization of magnetism in the different samples studied in this work, and in particular, demonstrate that the parent samples have unique compositions of excess Fe. In Fig. S3 we compare inelastic intensity at $\hbar\omega = 7.5$ meV, an energy at which a maximum in magnetic scattering is observed in the parent compounds and the magnetic resonance occurs in the superconducting material. We present slices in both the $(HK0)$ and $(H0L)$ zones, except for $\text{Fe}_{1.06}\text{Te}$ which was only measured in the $(H0L)$ zone. In both $\text{Fe}_{1.06}\text{Te}$ and $\text{Fe}_{1.1}\text{Te}$ we observe “rods” of magnetic scattering along l at $h \approx \pm 0.5$, with broad maxima around half-integer l . Weak diffuse scattering centered at $\mathbf{Q} = (0.5, 0, 0)$ in the $(HK0)$ zone observed in $\text{Fe}_{1.1}\text{Te}$ is a signature of ferromagnetic-square-plaquette-type correlations [see Ref. 34 in main text]. In superconducting $\text{FeTe}_{0.55}\text{Se}_{0.45}$, magnetic scattering is strongest near $\mathbf{Q} = (0.5, 0.5, 0)$, Fig. S3e, indicating a different type of plaquette correlations [35], and therefore only a weak diffuse “tail” signal is observed in the $(H0L)$ zone (Fig. S3f). In Figs. S3g-h, we present structural and magnetic order parameters as a function of temperature, on warming and cooling for $\text{Fe}_{1.1}\text{Te}$, and on warming for $\text{Fe}_{1.06}\text{Te}$. Samples were oriented in the $(H0L)$ zone, where (100) and $(\approx 1.5, 0, 0.5)$ were measured on HYSPEC with a small range of sample rotation. We present the integrated intensity around these two peaks, which illustrates the ordering temperatures of the bond-order wave and antiferromagnetism.

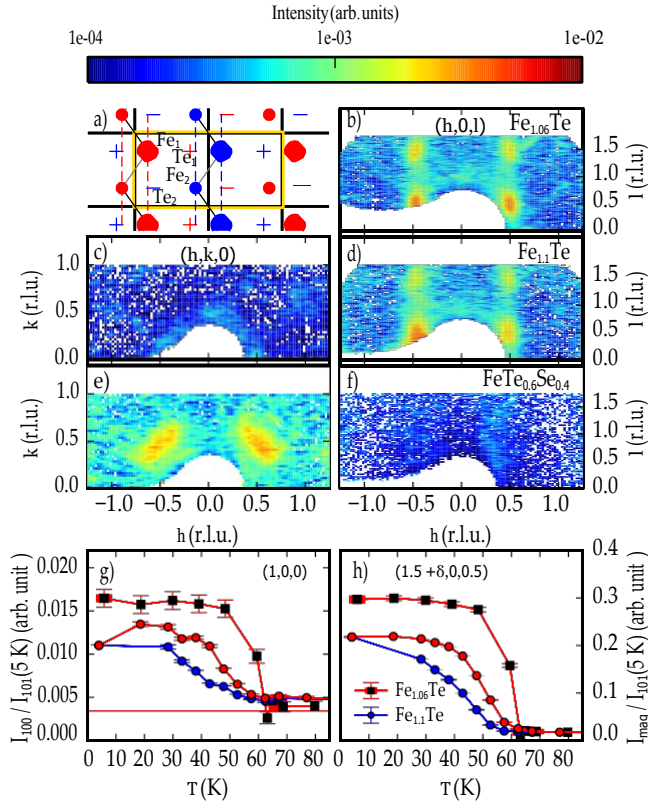


Figure S3. (a) Schematics from LDA frozen phonon calculations illustrating correlation between Fe atoms displacement along the x direction in the $a - b$ plane and the size of the local magnetic moment. Plus (minus) symbols indicate Te atoms above (below) the Fe plane. Circles represent Fe atoms, where diameter indicates magnetic moment. (b – f) Inelastic neutron scattering maps at $\hbar\omega = 7.5$ meV, 5 K: (b), (d), and (f) show $\text{Fe}_{1.06}\text{Te}$, $\text{Fe}_{1.1}\text{Te}$, and $\text{FeTe}_{0.55}\text{Se}_{0.45}$ in the $(H, 0, L)$ zone, respectively, and (c) and (e) show $\text{FeTe}_{0.55}\text{Se}_{0.45}$ and $\text{Fe}_{1.1}\text{Te}$ in the $(H, K, 0)$ zone, respectively. (g – h) Order parameters for $\text{Fe}_{1.06}\text{Te}$ and $\text{Fe}_{1.1}\text{Te}$: integrated intensity around (g) $(1, 0, 0)$ and (h) $(\approx 1.5, 0, 0.5)$ for $\text{Fe}_{1.06}\text{Te}$ (squares) on warming and $\text{Fe}_{1.1}\text{Te}$ (circles) on both cooling and warming. Error bars in all figures represent one standard deviation.

3. Additional analyses of the line cuts of the data in the $(hk0)$ plane shown in Figure 2 of the main text.

Presented in Figure S4 are the line cuts of the data shown in Figure 2 of the main text, which compare the transverse velocity of the allowed phonons near $(2n, 0, 0)$ lattice Bragg peaks and that of the forbidden mode near $(2n + 1, 0, 0)$ positions in the $(hk0)$ scattering plane in $\text{Fe}_{1.1}\text{Te}$ and $\text{FeTe}_{0.55}\text{Se}_{0.45}$. The data were fit to the two Gaussian peaks, equally offset from the center (the Bragg position). The fitted peak positions correspond to nearly identical transverse acoustic velocities in both cases. In $\text{Fe}_{1.1}\text{Te}$ (a) the transverse phonon velocity is $25.5(8)$ meV/r.l.u. and that of the forbidden mode is $25.5(29)$ meV/r.l.u., while these are $34(2)$ meV/r.l.u. and $30(3)$, respectively, in $\text{FeTe}_{0.55}$

Se_{0.45} (b). It should be noted that velocities refined from the line cuts measured in FeTe_{0.55}Se_{0.45} (b) with $E_i = 50$ meV are less reliable because of the significant systematic error associated with rather coarse energy resolution of this configuration. Nevertheless, the refined transverse velocity of the forbidden mode compares favorably with that obtained from the transverse scans shown in Figure 3 of the main text, $v = 31.7(15)$ meV/r.l.u., where data collected using $E_i = 24$ meV is shown.

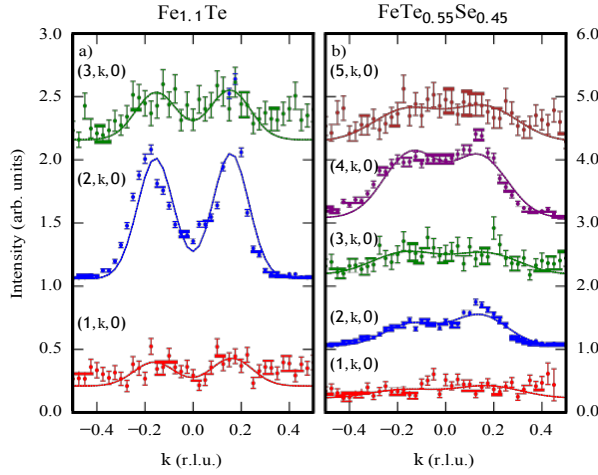


Figure S4. Transverse line cuts quantifying the sound velocity near the forbidden, $(2n + 1, 0, 0)$, and the allowed, $(2n, 0, 0)$, lattice Bragg positions in Fe_{1.1}Te (a) and FeTe_{0.55}Se_{0.45} (b). In all figures error bars represent one standard deviation.

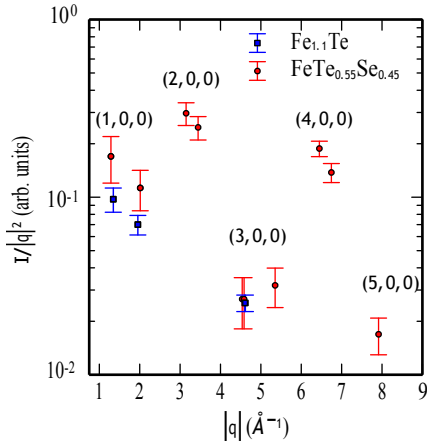


Figure S5. The wave-vector-normalized intensity of phonon at symmetry-equivalent positions near allowed and forbidden Bragg peaks in Fe_{1.1}Te and Fe_{1.1}Te_{0.55}Se_{0.45} in (hk0) zone, obtained from the line fits of longitudinal scans shown in Figure 2, (c) and (d) of the main text. Note the logarithmic intensity scale.

Figure S5 presents the wave-vector-normalized phonon intensity, $I(Q)/Q^2$ at symmetry-equivalent positions near the forbidden Bragg peaks in Fe_{1.1}Te, and allowed

and forbidden peaks in $\text{Fe}_{1.1}\text{Te}_{0.55}\text{Se}_{0.45}$ in (hk0) zone, obtained by fitting the longitudinal line scans shown in Figure 2, (c) and (d) of the main text. As expected, this quantity is roughly constant for an allowed phonon near $(2n, 0, 0)$. However, it decreases markedly for the forbidden mode, even though the absolute intensity increases with Q . This increase, however, is noticeably slower than $\sim Q^2$ expected for an acoustic phonon at symmetry-equivalent positions in reciprocal lattice.

4. Analysis of the acoustic mode intensity in $\text{Fe}_{1.06}\text{Te}$ and $\text{Fe}_{1.1}\text{Te}$ and in (hk0) zone

Here we present analyses of the (100) forbidden-phonon dispersion in $\text{Fe}_{1.06}\text{Te}$, $\text{Fe}_{1.1}\text{Te}$, and $\text{FeTe}_{0.55}\text{Se}_{0.45}$ in the (hk0) scattering plane similar to that in Fig. 3 of the main text. In all cases there is no decrease of the integrated χ'' intensity with the decreasing energy [i.e. \mathbf{Q} moving towards (100)].

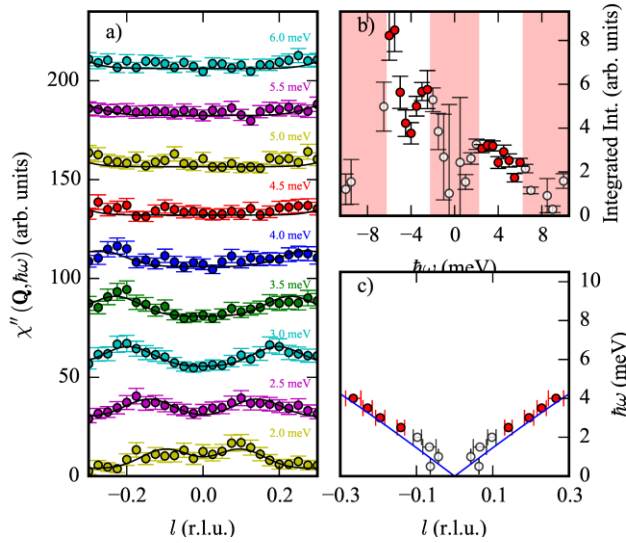


Figure S6. (100) mode in $\text{Fe}_{1.1}\text{Te}$ in the (h0l) scattering plane. In all figures error bars represent one standard deviation.

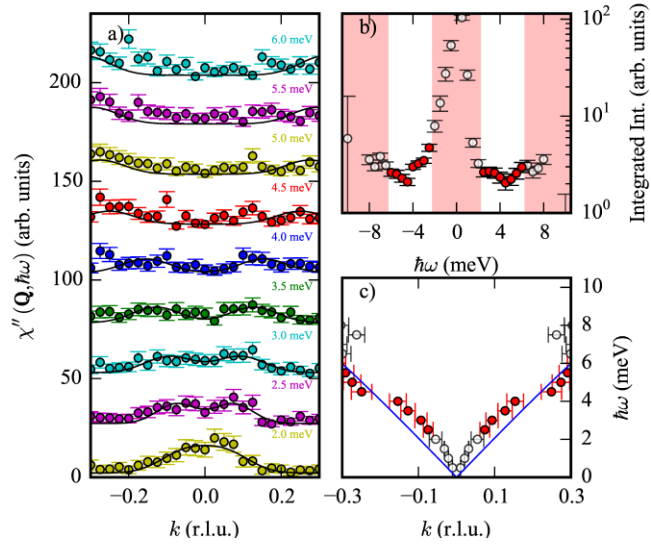


Figure S7. (100) mode in $\text{Fe}_{1.1}\text{Te}$ in the $(hk0)$ scattering plane.

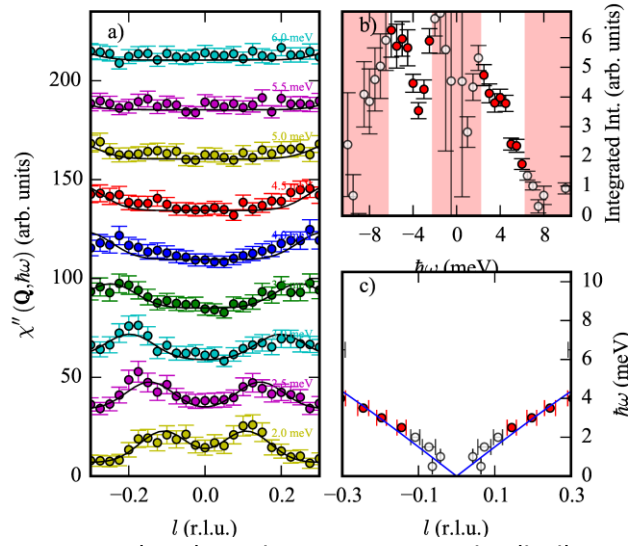


Figure S8. (100) mode in $\text{Fe}_{1.06}\text{Te}$ in the $(h0l)$ scattering plane.

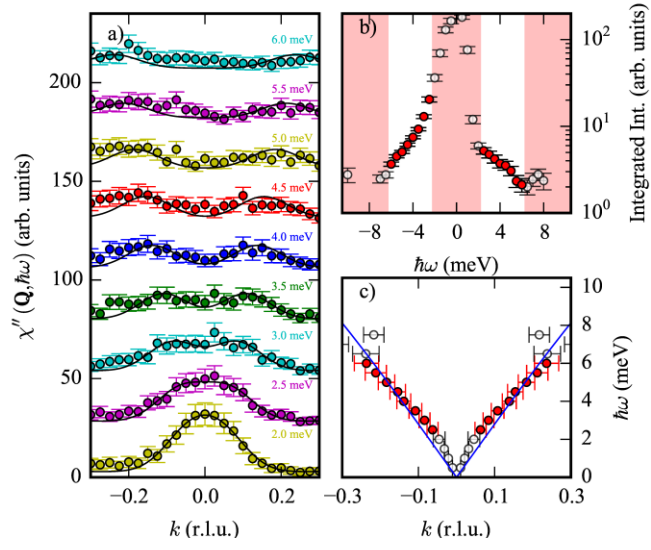


Figure S9. (100) mode in FeTe_{0.55}Se_{0.45} in the (hk0) scattering plane.